# The Great PV Ceph Outflow: A Case Study in Outflow-Cloud Interaction

Héctor G. Arce<sup>1</sup> & Alyssa A. Goodman

Harvard-Smithsonian Center for Astrophysics, 60 Garden St., Cambridge, MA 02138

harce@cfa.harvard.edu, agoodman@cfa.harvard.edu

#### ABSTRACT

We present a set of detailed molecular line maps of the region associated with the giant Herbig-Haro flow HH 315, from the young star PV Cephei, aimed at studying the outflow-cloud interaction. Our study clearly shows that the HH 315 flow is effecting the kinematics of its surrounding medium, and has been able to redistribute considerable amounts of the surrounding medium-density  $(\sim 10^3 \ {\rm cm}^{-3})$  gas in its star-forming core as well at parsec-scale distances from the source. The single-dish observations include a map of the outflow in the <sup>12</sup>CO(2-1) line, with a beam size of 27", and more extended maps of the outflow region in the  $^{12}CO(1-0)$  and  $^{13}CO(1-0)$  lines, with 45" and 47" beam sizes, respectively. A companion paper to this one presents higher-resolution (IRAM 30-m) observations, and discusses their implications (Arce & Goodman 2002). The giant molecular outflow HH 315 is a highly asymmetric bipolar flow with a projected linear extent of about 2 pc. Our results indicate that the two outflow lobes are each interacting with the ambient medium in different ways. The southern (redshifted) lobe, with a mass of 1.8  $M_{\odot}$ , interacts with a dense ambient medium, very close to the young stellar outflow source, and its kinetic energy is comparable to both the turbulent and gravitational binding energy of its host cloud (of order  $10^{44}$  erg). In addition, we find evidence that the southern lobe is responsible for the creation of a cavity in the <sup>13</sup>CO emission. In contrast, the northern (mainly blueshifted) outflow lobe, with a total mass of 4.8  $M_{\odot}$ , extends farther from PV Ceph and interacts with ambient gas much less dense than the southern lobe. There is very little <sup>13</sup>CO emission north of the outflow source, and the only prominent <sup>13</sup>CO emission is a shell-like structure coincident with the outer edge of the northern lobe, about 1.2 pc northwest of PV Ceph. It appears that the northern lobe of the HH 315 outflow has been able to "push" aside a substantial fraction of the gas in the area, piling it in a dense shell-like structure at its edges. In addition, we find that about 50% of the gas in the region of the northern lobe has been put in motion by the outflow, and that the northern outflow lobe is responsible for a velocity gradient in the ambient gas.

Subject headings: ISM: jets and outflows — ISM: Herbig-Haro Objects — ISM: individual (HH 315, PV Cephei) — ISM: clouds — stars: formation

#### 1. Introduction

As stars form inside molecular clouds, they gravitationally gather gas from their surroundings, while simultaneously spurting out vast amounts of mass in a bipolar flow. The young stellar wind may reveal itself in different ways. Among the many manifestations of a nascent star's mass loss process are Herbig-Haro (HH) objects and molecular outflows. An HH object is a nebulous knot, mainly seen at optical wavelengths, which delineates the shock arising from the interaction of a high-velocity flow of gas ejected by a young stellar object (YSO) and the ambient medium. A chain of these HH objects (or knots) is usually referred as an HH flow. One or more shocks associated with an outflow can accelerate entrained gas to velocities greater than those of the quiescent cloud, transferring momentum and energy into the host molecular cloud, thereby producing a molecular outflow.

Since their discovery, molecular outflows have been thought to supply their host cloud with energy (e.g., Norman & Silk 1980). Yet, the (past) notion that outflows rarely extended to more than 1 pc in length, and that they only effected a minor volume of the cloud, made it difficult to believe that stellar outflows could be important to the energetics of their host cloud. This picture is now changing. Recent studies have shown that outflows from young stars have an enormous potential to influence their parent cloud's structure and lifetime. Optical and near-infrared observations have revealed that giant —parsec-scale— HH flows exist and that they are common (Eislöffel & Mundt 1997; Devine et al. 1997; Reipurth, Bally, & Devine 1997, hereafter RBD; Mader et al. 1999; Eislöffel 2000; Stanke, McCaughrean, & Zinnecker 2000). Giant HH flows have sizes about an order of magnitude larger than the cloud cores from which they originate, and many are found to extend to distances well outside the boundary of their parent dark cloud. The colossal size of a giant HH flow enables it to entrain molecular material at parsec-scale distances from the source, and thus it may effect the kinematics and density of a substantial volume of its parent molecular cloud.

In order to study the effects an outflow has on its environment's kinematic and density structure, it is imperative to observe a large area of the cloud gas surrounding the outflow, in addition to the outflow itself. The observations should preferably be of more than one

<sup>&</sup>lt;sup>1</sup>Now at: California Institute of Technology, Astronomy Department, MS 105-24, Pasadena, CA 91125.
New e-mail: harce@astro.caltech.edu

molecular line transition, probing a range of densities, and at least one of the lines should be relatively optically thin, in order to take line opacity into account. Also, if one is to avoid source confusion, one should study regions with a very low density of young stellar objects.

The HH 315 flow, from the young star PV Cephei (or PV Ceph) is a perfect laboratory to study outflow-cloud interaction as each outflow lobe interacts with drastically different environments. In addition, there is little chance for source confusion in the area near HH 315 since there are no known outflow-powering YSOs, other than PV Ceph, in a 30' radius centered on PV Ceph.

The giant HH 315 flow was discovered independently by Gómez, Kenyon & Whitney (1997, hereafter GKW) and RBD. The presumed source of the HH 315 flow is PV Cephei, a variable Herbig Ae/Be pre-main sequence star located at the northeastern edge of the L1158 and L1155 group of dark clouds, which is believed to be at a distance of 500 pc (Cohen et al. 1981). A brief literature review of the observations of PV Ceph is given by GKW. The HH 315 flow (see Figure 1) consists of six major condensations (which are named knot A, B, C, D, E, F), and each major condensation (or knot) is made of two or more individual small HH knots (identified F1, F2, F3, etc.). In addition, a group of knots, which were originally discovered by Neckel et al. (1987), are seen 20" to 55" north of PV Ceph, and are identified as HH 215. RBD state that HH 215 and HH 315 are all part of a single 2.6 pc-long (in projection) HH flow which, all together, are commonly referred to as the HH 315 flow. The northern lobe of the HH 315 flow is made of HH 215, and knots A, B, and C. The southern lobe is made of knots D, E, and F (see Figure 1). The spectra of several knots (Devine 1997) show that the northern lobe is blueshifted and the southern lobe is redshifted.

RBD affirm that the distances from the source to knot A, B, and C are within 10% of the distance from the source to knots D, E, and F, respectively (see Figure 1). They argue that the coincidence in the distance from the source to the knots, and the S-shaped point symmetry of the two lobes around the source (see below) are evidence that the six knots come from three major mass ejection eruptions. In this picture the oldest eruption is responsible for the C-F knot pair, followed by the eruption responsible for the B-E pair, which is followed by the eruption responsible for the A-D pair. The most recent eruption is responsible for the HH 215 knots, and a counter-knot to HH 215 is not observed south of PV Ceph presumably because is heavily obscured by the dense gas near PV Ceph (RBD). Assuming a tangential velocity of 200 km s<sup>-1</sup> for each knot, RBD estimate that the major eruptions in PV Ceph have occurred every 2000 yr, starting with the C-F eruption about 6500 yr ago.

A very peculiar aspect of HH 315 is that the knots trace a roughly sinusoidal path, or S-shaped point symmetry around PV Ceph. RBD and GKW argue that this particular flow

morphology strongly suggests that the ejection axis of PV Ceph is wandering or precessing (i.e., changes over time). GKW modeled the HH 315 flow with a simple precessing jet model. In their model the jet axis precesses on a cone with full opening angle,  $\theta$ , inclined to the plane of the sky at an angle i, and the jet is assumed to have a constant velocity and a constant precession velocity. GKW state that assuming a jet velocity of 200 km s<sup>-1</sup>, with  $i \sim 10^{\circ}$ ,  $\theta \sim 45^{\circ}$ , and a precession period of about 8300 yr their models can produce a jet consistent with the HH 315 flow morphology. It is also possible to explain the knot position angles and symmetries with a model where PV Ceph is moving at a substantial velocity ( $\sim 10 \text{ km s}^{-1}$ ) and pairs of knots are emitted at varying angles as the source travels through space (see Goodman & Arce 2002).

The molecular outflow associated with the HH 315 flow was first observed by Levreault (1984). The low resolution  $^{12}\text{CO}(1-0)$  map of Levreault (1984) shows that the HH 315 molecular outflow is asymmetric. The redshifted lobe has a circular morphology with a diameter of  $\sim 0.3$  pc, and the blueshifted lobe has an elongated morphology which extends up to  $\sim 1.2$  pc northwest from PV Ceph. Here we present new, more sensitive, and higher spatial resolution  $^{12}\text{CO}(2-1)$ ,  $^{12}\text{CO}(1-0)$ , and  $^{13}\text{CO}(1-0)$  observations of the HH 315 molecular outflow, its surroundings, and a large fraction of its parent dark cloud. Our analysis focuses on the effects of the giant HH 315 outflow on its host cloud.

In Section 2 we give a description of our observations, and in Section 3 we describe our results. In Section 4 we discuss the mass and energetics of the HH 315 flow and the effects that the HH 315 flow has on its parent cloud. We devote Section 5 to our conclusions. A study of the kinematics of the HH 315 outflow and the entrainment mechanism is discussed in Arce & Goodman (2002, hereafter Paper II), using even higher angular and velocity resolution (IRAM 30 m telescope) molecular line data of the gas immediately surrounding PV Ceph (the HH 215 region) and the HH 315B and HH 315C optical knots.

# 2. Observations

# 2.1. <sup>12</sup>CO(2–1) Data

The <sup>12</sup>CO(2–1) line data were obtained using the on-the-fly mapping technique at the National Radio Astronomy Observatory (NRAO) 12 m telescope on Kitt Peak, Arizona, in December 1998. At the observed frequency of 230 GHz, the telescope's half-power beam width, main beam efficiency, and aperture efficiency are 27", 0.32 and 0.44, respectively. The spectrometer used was a filter bank with 250 kHz resolution, with two independent sections of 128 channels each. The filter bank was put in parallel configuration, in which

each of the two sections received independent signals with a different polarization. The parallel configuration was chosen so that ultimately the two polarizations could be averaged to produce better signal-to-noise spectra. At a frequency of 230 GHz, the resultant velocity resolution for this setup is  $0.65 \text{ km s}^{-1}$ .

The on-the-fly (OTF) mapping technique was used to observe an area of about 215□′ surrounding the HH 315 flow. The OTF technique allowed the extended area to be mapped in a more efficient way than the conventional point-by-point mapping. The telescope in OTF mode moved across the source at a constant speed of 30" s<sup>-1</sup>, while a spectrum was acquired every 0.1 seconds. In order to map the desired area more efficiently, the total area was mapped by combining three overlapping regions of different sizes and orientation. The largest region (hereafter central region) has a size of  $11' \times 13'$ , oriented at a position angle of -26° centered around the position of PV Ceph, at R.A. 20<sup>h</sup>45<sup>m</sup>23<sup>s</sup>.3, decl. 67°46′36″ (B1950). The second region (hereafter SE region) is a rectangle of about  $10.5' \times 6.5'$ , and it is centered southeast of PV Ceph at R.A.  $20^h45^m58^s$ , decl.  $67^{\circ}40'15''$  (B1950). The third region (hereafter NW region) is a rectangle, of about  $10.5' \times 6.5'$ , and it is centered northwest of PV Ceph at R.A.  $20^h44^m52^s$ , decl.  $67^{\circ}53'00''$  (B1950). Each region was scanned in both the directions perpendicular and parallel to its long axis. The separation, in the direction perpendicular to the scanning direction, between subsequent rows was 7.2" for the central region and 8" for the SE and NW regions. The telescope was pointed to an OFF position after every other row, where it would observe the OFF position for 10 sec and then vane calibrate for 5 sec. We used a different OFF position, depending on the region observed in order to reduce the time needed to move from the "ON" area to the OFF position. The central region and the NW region used the same OFF position, located at R.A.  $20^h45^m26^s$ , Dec.  $67^{\circ}56'22''$  (B1950) and for the SE region we use a different OFF, located at R.A.  $20^{h}45^{m}26^{s}$ , Dec. 67°56′22″ (B1950). Deep observations at the OFF positions show that there is very faint emission at these positions in the velocity range between 0.5 and 3.0 km s<sup>-1</sup>, with  $0.1 \lesssim T_A^* \lesssim$  0.3 K, and no emission greater than 0.1 K at other velocities. Most of the outflow emission is at velocities less than and greater than 0.5 and  $3.0 \text{ km s}^{-1}$ , respectively. Therefore, the very small amount of emission at velocities between 0.5 and  $3.0~{\rm km~s^{-1}}$  at the OFF positions does not affect our outflow data. The different regions were observed several times to improve the signal-to-noise in the spectra. The system temperature was measured to be in the range between 350 and 800 K. Our goal was to maintain a constant noise level through the whole map, so regions that were mapped with a higher system temperature were given comparatively more integration time.

The raw OTF data were reduced using various AIPS OTF tasks. A first-order baseline was fitted and subtracted to each spectrum, and the two polarizations were averaged. The different mapped regions were combined and averaged. The map was then convolved onto

a grid with 14" pixels (Nyquist sampled). The resultant RMS noise in each 0.65 km s<sup>-1</sup> channel was 0.1 K, for most (non border) spectra. The intensity scale of the spectral data presented in this chapter is in units of  $T_A^*$  (Kutner & Ulich 1981) unless otherwise stated.

# 2.2. $^{12}CO(1-0)$ , $^{13}CO(1-0)$ , and $C^{18}O(1-0)$ Data

In order to study the effect of the HH 315 outflow on a larger scale and to obtain a better estimate of the outflow mass, we observed the  ${}^{12}CO(1-0)$  line in a region 17.6' by 29.3' and the  $^{13}$ CO line in a region 11.7′ by 23.5′, both along a position angle of -30°, surrounding PV Ceph. The data were obtained using the SEQUOIA 16 element focal plane array receiver of the Five College Radio Astronomy Observatory (FCRAO) 14 m telescope. The observations were done over the course of three different observing rounds, which took place in April 1999, December 1999, and February 2000. The backend used for observing both lines was the Focal Plane Array Autocorrelator Spectrometer, with a channel spacing of 78 kHz (0.21 km s<sup>-1</sup>) for <sup>12</sup>CO(1–0), at a frequency of 115 GHz, and a channel spacing of 20 kHz (0.05 km s<sup>-1</sup>) for <sup>13</sup>CO(1–0), at a frequency of 110 GHz. The <sup>12</sup>CO(1–0) line was observed in position switching mode, with a single OFF position located at R.A.  $20^h46^m50^s$ , decl.  $68^{\circ}01'36''$ (B1950). Observations at the OFF position reveal no significant ( $T_A^* \lesssim 0.2$  K) emission. The  $^{13}$ CO line was observed in frequency switching mode. The telescope half-power beam widths for the  $^{12}CO(1-0)$  and  $^{13}CO(1-0)$  lines are 45" and 47", and the main beam efficiencies are 0.45 and 0.54, respectively. Both lines were observed on a 22" grid (Nyquist sampled), and with an integration time of 100 sec for each position. The system temperature of our <sup>13</sup>CO(1-0) observations was about 250 K, and for our <sup>12</sup>CO(1–0) observations it ranged between 500 and 900 K.

Observations of the  $C^{18}O(1-0)$  emission were also made using the same telescope and backend configuration as the  $^{13}CO(1-0)$  observations. We made one  $5.5' \times 5.5'$  FCRAO-SEQUOIA footprint centered at the position of PV Ceph. The telescope half-power beam width and main beam efficiency for  $C^{18}O(1-0)$ , at a frequency of 109 GHz, are 47" and 0.54, respectively. Each position was observed for 210 sec, with a system temperature of about 280 K.

The  $^{12}$ CO(1–0) and  $^{13}$ CO(1–0) data were reduced with the CLASS and MIRIAD packages. For the purpose of obtaining the molecular gas mass (see §3.4), the original spectra from both lines were smoothed and resampled to a channel spacing of 0.22 km s<sup>-1</sup>. The spectra were spatially linearly interpolated and a data cube of 11.5" pixels was produced for each line. The data cube was then smoothed by convolving it with a Gaussian with a FWHM of 46". The resultant RMS noise of the spectra in the  $^{12}$ CO(1–0) and  $^{13}$ CO smoothed maps

is 0.14 K and 0.04 K for each  $0.22 \text{ km s}^{-1}$  channel, respectively. Interpolating the  $^{12}\text{CO}(1-0)$  and the  $^{13}\text{CO}$  data to this common position-velocity grid allowed us to use them in concert when calculating the mass estimates presented in §3.4.

#### 3. Results

# 3.1. <sup>12</sup>CO(2–1) Maps

# 3.1.1. Integrated Intensity Map

In Figure 1 we show the integrated velocity map of the molecular outflow associated with the HH 315 flow, created by integrating over wide blue- and red-shifted velocity ranges. The integrated velocity map is overlaid on an optical image of the region (from RBD). The large extent of the flow is clearly seen. The blueshifted lobe (northwest of PV Ceph) is about 0.6 pc wide and 0.8 pc long, and the redshifted lobe is about 0.3 pc wide and 0.5 pc long.<sup>2</sup> Another striking aspect of this molecular outflow, besides its large extent, is the difference in size and morphology of the two outflow lobes. The blue lobe shows a bow shock-like appearance, with an axis of P.A.  $\sim -26^{\circ}$ , and with its northern edge coincident with the optical knot HH 315C. Most of the blueshifted emission resides in a region near the optical knot HH 315C and HH 315B, and does not extend all the way to source. In contrast, most of the red lobe's emission is concentrated in a collimated north-south structure that extends from PV Ceph south about 0.3 pc. The redshifted lobe also includes a more extended, wider region of low intensity emission which has its southern edge near the position of the optical knot HH 315D. In addition to the morphological differences, the lobes also have different maximum outflow velocities. Our large scale map, shows <sup>12</sup>CO(2-1) blueshifted lobe velocities up to  $\sim 16.0 \text{ km s}^{-1}$  away from the central velocity of the ambient cloud. On the other hand, the <sup>12</sup>CO(2–1) red lobe shows maximum outflow velocities of only up to  $\sim 6.5 \; {\rm km \; s^{-1}}.$ 

Levreault (1984) suggested that the asymmetry in the lobes' morphology and velocity distribution is due to the underlying density distribution in the PV Ceph region. Our <sup>13</sup>CO(1–0) map of the region (see §3.2) shows that there is indeed a drastic difference in the ambient density between north and south of PV Ceph. The outflow-cloud interaction should be a momentum-conserving interaction, thus the difference in ambient density may partly explain the asymmetry between the molecular outflow lobes' morphology and kinematics.

<sup>&</sup>lt;sup>2</sup>The full flow, measured as the distance between the outermost HH knots, is 2.6 pc long (see Figure 1).

It is interesting to note that although the *molecular* outflow shows a high degree of asymmetry between its two lobes, the lobes of the HH flow are highly symmetric about the source (see Figure 1). A clump of gas propagating through the interstellar medium (e.g., an HH knot) will decelerate by drag forces and the deceleration is expected to be proportional to the density of the ambient medium (De Young & Axford 1967; Cantó et al. 1998; Cabrit & Raga 2000). Thus, one would expect the southern HH knots of HH 315 to decelerate more than the northern HH knots, resulting in an asymmetric HH flow. We believe that HH 315 is able to keep its high degree of symmetry because the southern HH knots only travel a short distance inside the high density regions of the molecular cloud. The southern HH knots must travel through dense gas once they are ejected near the source. However, our high-resolution data (see Paper II for details) indicate that the HH knots are quickly out of the molecular cloud and coasting through low-density atomic gas by the time they reach the position of HH 315E (at a distance of 0.9 pc from PV Ceph).

#### 3.1.2. Channel Maps

In Figure 2 we show 12 velocity-binned ("channel") maps of the <sup>12</sup>CO(2–1) data. It is clear that most of the <sup>12</sup>CO(2–1) emission comes from the (0.65 km s<sup>-1</sup>-wide) velocity channels centered at 0.38, 1.03, 1.68, 2.33, and 2.98 km s<sup>-1</sup>. The central velocity of the ambient gas associated with PV Ceph is about 2.5 km s<sup>-1</sup> (see Cohen et al. 1981, and §3.3), thus most of the ambient cloud emission surrounding PV Ceph comes from the channels centered at 2.33 and 2.98 km s<sup>-1</sup>. The emission at these two velocity channels concentrates around (and south of) the location of PV Ceph, but there is also a local peak in the emission about 9′ northwest of the source.

It should be noted that in our  $^{12}\text{CO}(2\text{--}1)$  map we also detect emission from another cloud which is unrelated to the cloud associated with the young star PV Ceph. This cloud (hereafter cloud X) contributes a major fraction of the total emission seen at  $v_{chan} = 1.03 \text{ km s}^{-1}$ , and is also detected at  $v_{chan} = 0.38$  and  $v_{chan} = -0.28 \text{ km s}^{-1}$  (see Figure 2). Cloud X has a filamentary structure with a northwest-southeast long axis, most clearly seen in  $v_{chan} = 0.38 \text{ km s}^{-1}$ , and may also be seen, less clearly at  $v_{chan} = 1.03 \text{ and } -0.28 \text{ km s}^{-1}$ .

The blueshifted lobe of the PV Ceph molecular outflow is easily discernible at  $v_{chan} = 0.38 \text{ km s}^{-1}$ , where the structure of the  $^{12}\text{CO}(2-1)$  gas about 9' northwest of the source, has a bow shock-like appearance. This bow-shock-like structure is coincident with the position of the HH 315C optical knot (see also Figure 1), and can also be clearly seen at the velocity channels centered at -0.28, -0.93, and -1.58 km s<sup>-1</sup>, and less clearly at  $v_{chan} = -2.23 \text{ km s}^{-1}$ . At  $v_{chan} = -0.28 \text{ km s}^{-1}$ , this structure is about 0.5 pc wide and 0.75 pc long.

This blueshifted CO bow morphology arises from the interaction between a bow shock from an underlying jet (i.e., the HH 315C optical knot) and the ambient gas (see Paper II for details). The average axis of the HH 315 flow is believed to be close to the plane of the sky (GKW). Thus, it is reasonable to assume that the redshifted emission at a distance of  $\sim 9'$  northwest of the source, near the position of the HH 315C knot, at  $v_{chan} = 2.98$  and  $v_{chan} = 3.63$  km s<sup>-1</sup> (see Figure 2), comes from the gas accelerated away from us, on the "back side" of the HH 315C bow shock (see Paper II).

At higher blueshifted velocity channels ( $v_{chan} = -0.93, -1.58, -2.23 \,\mathrm{km \, s^{-1}}$ ) some of the bow shock-like structure can be seen near HH 315C, in addition to emission at the positions of the optical knots HH 315A and HH 315B. The blueshifted gas emission near HH 315A is very faint, and dispersed. On the other hand, the  $^{12}\mathrm{CO}(2-1)$  associated with the HH 315B blueshifted optical knot is relatively strong and has a defined knot-like structure, with a peak  $^{12}\mathrm{CO}(2-1)$  emission coincident with the location of the peak in the HH 315B optical emission (see Figures 4.1 and 4.2).

The redshifted velocity channel maps show a very different morphology than the blueshifted channels. At  $v_{chan} \geq 3.63$  km s<sup>-1</sup> most of the  $^{12}\text{CO}(2-1)$  emission is limited to a small region close to PV Ceph. In  $v_{chan} = 3.63$  km s<sup>-1</sup>, in addition there is also some faint  $^{12}\text{CO}(2-1)$  emission near the position of the redshifted optical knot HH 315D, and some faint emission near HH 315C. At  $v_{chan} \geq 4.28$  all of the emission is concentrated very close to the source, mostly in a north-south structure.

The  $^{12}\mathrm{CO}(1-0)$  velocity maps show basically the same structure as the  $^{12}\mathrm{CO}(2-1)$  maps. Our  $^{12}\mathrm{CO}(1-0)$  data set is not as sensitive as our  $^{12}\mathrm{CO}(2-1)$  data set, thus for illustrative purposes we only show the  $^{12}\mathrm{CO}(2-1)$  maps.

# 3.2. <sup>13</sup>CO(1–0) Maps

Most of the  $^{13}$ CO(1–0) emission in this region of the sky is optically thin, and thus is a good probe of the structure of the medium density ( $n \sim 10^3$  cm<sup>-3</sup>) gas. The  $^{13}$ CO(1–0) opacity may be estimated with C<sup>18</sup>O(1–0) observations of the same region (e.g., Heyer et al. 1987). Our 5.5' by 5.5' map of C<sup>18</sup>O(1–0) centered on PV Ceph shows that the C<sup>18</sup>O emission is concentrated around the young star, at velocities between 2.1 and 3.2 km s<sup>-1</sup>, and that there is no detectable emission at other velocities nor at distances greater than 2' from PV Ceph. The maximum emission in our  $^{13}$ CO map (Figure 3) is near PV Ceph, and hence it is fair to assume that all other local peaks in the  $^{13}$ CO emission far from PV Ceph are less optically thick than the emission near PV Ceph. Thus, we assume that the  $^{13}$ CO

emission in the area we studied is only mildly optically thick very near PV Ceph and other local <sup>13</sup>CO maxima (and only at ambient cloud velocities) and it is optically thin everywhere else. On the other hand, the <sup>12</sup>CO emission is optically thick almost everywhere (see §3.4), so the <sup>13</sup>CO emission is a much better probe of the cloud structure.

In Figure 3 we show six <sup>13</sup>CO maps, integrated over six different velocity ranges. It should be noted that the velocity ranges shown in each panel of Figure 3 are not of equal width. The velocity ranges were chosen to group different channels with similar <sup>13</sup>CO emission structure.

The first map is integrated over the velocity range of  $0.50 < v < 1.50 \,\mathrm{km \, s^{-1}}$  (Figure 3a). At these velocities most of the emission is concentrated west and northwest of PV Ceph. An interesting feature seen in Figure 3a is the shell-like structure about 9' northwest of PV Ceph. This structure encloses the bow shock-like blueshifted  $^{12}\mathrm{CO}(2-1)$  lobe of the HH 315 molecular outflow (see Figures 1 and 2). It appears that the blueshifted lobe of the HH 315 flow has "pushed" aside the  $^{13}\mathrm{CO}$ , piling the gas in a shell-like structure at the edges of the blue lobe (see §4.2.2 for a discussion of this). Note that Cloud X can also be seen in  $^{13}\mathrm{CO}$  emission at these velocities.

Figures 3b and 3c show the  $^{13}{\rm CO}$  integrated emission over the ranges  $1.50 < v < 1.84~{\rm km~s^{-1}}$  and  $1.84 < v < 2.17~{\rm km~s^{-1}}$ , respectively. The  $^{13}{\rm CO}$  emission in Figure 3b is concentrated near the western edge of our map. The  $^{13}{\rm CO}$  emission in Figure 3c is also mainly concentrated near the western edge of the map, but, it is more spread out (towards the east) than the emission seen in Figure 3b. It is at the velocities of Figure 3c ( $1.84 < v < 2.17~{\rm km~s^{-1}}$ ) where we start to detect  $^{13}{\rm CO}$  associated with the cloud that harbors PV Ceph (see below). The  $^{13}{\rm CO}$  emission over the velocity ranges  $2.17 < v < 2.61~{\rm km~s^{-1}}$  and  $2.61 < v < 3.05~{\rm km~s^{-1}}$  (Figures 3d and 3e, respectively) show the main  $^{13}{\rm CO}$  structure of the cloud associated with the PV Ceph young star. The cloud's northern edge is just north of PV Ceph, and the cloud extends mainly towards the south-southwest of the young star. The  $^{13}{\rm CO}$  structure at these velocities is very similar to the  $^{12}{\rm CO}(2-1)$  structures seen at  $v_{chan} = 2.33$  and  $2.98~{\rm km~s^{-1}}$  (see Figure 2).

In Figure 3f we show the  $^{13}$ CO integrated intensity map over the velocity range 3.05 <  $v < 3.48 \rm ~km~s^{-1}$ , which reveals the most redshifted  $^{13}$ CO emission of our map. All of the  $^{13}$ CO emission is concentrated at the position of PV Ceph. This (unresolved) redshifted  $^{13}$ CO emission most probably comes from the medium density gas very near PV Ceph that has been accelerated by the HH 315 flow, or could also be due to the motion of PV Ceph (see Goodman & Arce 2002).

# 3.3. Dissecting the PV Ceph cloud

This subsection is intended to explain certain definitions we will use in the discussion that follows. Table 1 summarizes the definitions. We use the term "PV Ceph cloud" to refer to the cloud associated with the formation of the young star PV Ceph. We define the area and velocity limits of the PV Ceph cloud based on the <sup>13</sup>CO density and velocity structure. The central velocity of the PV Ceph cloud is 2.5 km s<sup>-1</sup> (see below, and Cohen et al. 1981), and the slowest (detected) redshifted molecular outflow velocity is 0.7 km s<sup>-1</sup> from the central velocity (see §3.4). Thus, we assume that 0.7 km s<sup>-1</sup> "blue-ward" and 0.7 km s<sup>-1</sup> "red-ward" of the central velocity, that is 1.8 < v < 3.2 km s<sup>-1</sup>, is the PV Ceph ambient cloud emission velocity range. It can be seen, from the <sup>13</sup>CO velocity channels, that it is at these velocities (1.8 < v < 3.2 km s<sup>-1</sup>) where there is <sup>13</sup>CO emission surrounding PV Ceph, which does not come from cloud X.

In Figure 4 we plot the  $^{13}$ CO position-velocity diagram of the mapped region, constructed by summing all spectra along an axis with a position angle of -26° over the whole width of the  $^{13}$ CO map. In Figure 4, the lower dashed box delimits the "PV Ceph Cloud," and the upper box defines the "North Cloud" (see Table 1). The box defining the PV Ceph cloud avoids the high-velocity  $^{13}$ CO feature at velocities greater than 3.2 km s $^{-1}$ . The box also avoids the  $^{13}$ CO emission at velocities lower than 1.8 km s $^{-1}$ . This emission at v < 1.8 km s $^{-1}$  is due to the  $^{13}$ CO clump south-southwest of PV Ceph (see Figure 3b) which is not part of the cloud associated with the formation of PV Ceph. The small velocity gradient south of PV Ceph is due to the kinematical distribution of the large scale  $^{13}$ CO emission in our map.

The integrated intensity map of the  $^{13}$ CO emission integrated over the PV Ceph ambient cloud velocities (1.8 < v < 3.2 km s $^{-1}$ ) is shown in Figure 5. The eastern and northern edges of the cloud are easily defined by the drop in  $^{13}$ CO emission (see Figure 5 and Table 1). The western and southern edges are not so clear, but it seems that R.A.  $20^h44^m32^s$  and decl.  $67^{\circ}36'30''$  (B1950) are reasonable choices for the eastern and southern edges, respectively. Figure 3 shows that most, if not all, of the  $^{13}$ CO emission at the defined velocities of the PV Ceph cloud (1.8 < v < 3.2 km s $^{-1}$ ) lies east of  $20^h44^m32^s$  and north of  $67^{\circ}36'30''$  (B1950).

In Figure 6 we show the area that we later use to calculate the mass of each molecular outflow lobe (see §3.4). We also show in Figure 6 (in dashed squares) the area used to estimate the velocity dependence of the  $^{12}CO(1-0)$  line opacity for each outflow lobe region, as discussed in §3.4. These smaller areas were chosen to have CO emission representative of the larger (outflow mass) areas, with as little contamination from unwanted cloud (and velocity) structures (e.g., cloud X) as possible. The "ambient" velocity for the Southern lobe,  $v_{amb,south}$ , is obtained from a two-Gaussian fit to the average  $^{12}CO(1-0)$  spectrum shown in

Figure 7a. The resultant value, for the narrow velocity component is  $v_{amb,south} = 2.5 \text{ km s}^{-1}$ .

It is evident that the molecular gas north of PV Ceph exhibits a large-scale velocity gradient. The overall gradient is in the sense that the  $^{12}$ CO and  $^{13}$ CO emission (with cloud-like morphology, presumably non-outflow gas) is shifted to the blue towards the north-northwest of the map (see Figures 2, 3, and 4). The central velocity of the northern lobe region (or "Northern Cloud") is  $v_{amb,north} = 1.5 \text{ km s}^{-1}$ , obtained using the same procedure described above for  $v_{amb,south}$ . We define the "Northern Cloud" to be in the velocity range  $0.8 < v < 2.2 \text{ km s}^{-1}$ , and to have an area shown by the box in Figure 6 (see also Table 1 and Figure 4). Later, we argue that the sense of the overall velocity gradient north of PV Ceph is not an accident, and that most of the mass in the northern cloud has been accelerated to blueshifted velocities by the HH 315 flow (see §4.2.2).

#### 3.4. Outflow Mass

#### 3.4.1. Procedure

To obtain the outflow mass we use the method described in §3.3.2 of Arce & Goodman (2001b, hereafter AG). This method, which is based on the method employed by Bally et al. (1999) and Yu et al. (1999), uses the  $^{12}CO(1-0)$  to  $^{13}CO(1-0)$  ratio to estimate the opacity in the  $^{12}CO(1-0)$  line, as a function of velocity. In most cases the  $^{12}CO(1-0)$  line is optically thick, and its opacity varies with velocity. Typically, the highest-velocity gas in the line wings is optically thin, and the optical depth increases as velocities approach the line center. Using an optically thick line, without properly correcting for its velocity-dependent opacity, will result in an underestimation of the the outflow mass, momentum and kinetic energy.

Here we give a brief description of the method used to estimate the outflow's mass (see AG for detail). First, in order to estimate the ratio of  $^{12}\text{CO}(1-0)$  to  $^{13}\text{CO}(1-0)$  as a function of velocity, we calculate average spectra of  $^{13}\text{CO}(1-0)$  and  $^{12}\text{CO}(1-0)$  over the region where most of the outflow emission is found (see Figure 6). We did this for two different regions, one for each outflow lobe. The average spectra of these two regions are shown in Figures 7a and 7b. In Figures 7c and 7d, we present the ratio of  $^{12}\text{CO}(1-0)$  to  $^{13}\text{CO}(1-0)$  main beam temperature  $(T_{mb}^{12}/T_{mb}^{13})$ , as a function of velocity for the average spectra of the south (red) and north (blue) lobe regions, respectively. The line ratios, hereafter denoted  $R_{12/13}(v)$ , were each fit with a second-order polynomial, as described below.

The fits to  $R_{12/13}(v)$  are each a truncated parabola with fixed minimum at the velocity where the average  $^{13}CO(1-0)$  spectrum peaks (this velocity is obtained by a two-Gaussian fit to each of the average  $^{13}CO$  spectra in Figures 7a and 7b). We exclude the three velocity

channels closest to the  $^{13}$ CO peak velocity from the fit to  $R_{12/13}(v)$ , as they are the velocities at which the  $^{13}$ CO emission might be slightly optically thick and where the  $^{12}$ CO emission is probably extremely optically thick. In both the red and the blue lobe's average  $^{13}$ CO spectra there are "contaminating" velocity components (e.g., cloud X; see Figure 7a and 7b). This contamination is at blueshifted velocities in the red lobe, and redshifted velocities for the blue lobe. So, after editing for this contamination, eliminating low signal-to-noise points, and the three points near the line core, we use only the points shown as filled symbols in Figures 7c and 7d in the final fits. The  $R_{12/13}(v)$  parabolic fit is then used to extrapolate  $R_{12/13}$  to the high-velocity wings of the outflow, where the  $^{13}$ CO line is too weak to be reliably detected (see below).

To calculate the outflow mass at a given (x, y) position, we directly use the <sup>13</sup>CO emission at low outflow velocities. At high outflow velocities, or wherever the <sup>13</sup>CO has not been reliably detected, we use the <sup>12</sup>CO(1–0) data and the fit to  $R_{12/13}(v)$ , to estimate the value of  $T_{mb}^{13}(v)$  at the given velocity and position, using the simple relation  $T_{mb}^{13}(x, y, v) = T_{mb}^{12}(x, y, v)[R_{12/13}(v)]^{-1}$ . The function  $R_{12/13}(v)$  is truncated at a value of 62, the assumed isotopic ratio (Langer & Penzias 1993). Once we estimate a value of  $T_{mb}^{13}(x, y, v)$ , we can obtain a value of the <sup>13</sup>CO opacity  $(\tau_{13}(x, y, v))$ , from which we then obtain a value of the <sup>13</sup>CO column density  $(N_{13}(x, y, v))$  and then the mass, using Equations 1, 3, and 4 of AG.

It should be noted that the  $^{13}\mathrm{CO}(1\text{--}0)$  excitation temperature  $(T_{ex})$  is needed in order to obtain an estimate of  $\tau_{13}(x,y,v)$  from  $T_{mb}^{13}(x,y,v)$  (see Equation 1 of AG). A value of  $T_{ex}$  is obtained by assuming that the excitation temperature for  $^{12}\mathrm{CO}(1\text{--}0)$  and  $^{13}\mathrm{CO}(1\text{--}0)$  are the same, and that the  $^{12}\mathrm{CO}(1\text{--}0)$  emission is optically thick at the line core. To obtain  $T_{ex}$ , we use an average spectrum of the  $^{12}\mathrm{CO}(1\text{--}0)$  data over a region 5.75′ by 9.58′, centered on  $20^h 45^m 24.7^s$ ,  $67^\circ 42' 19''$  (B1950). This region is where most of the  $^{13}\mathrm{CO}$  emission lies, and thus we are confident that the  $^{12}\mathrm{CO}$  emission at ambient cloud velocities in this region is extremely optically thick. The peak main beam temperature of the average spectrum is about 7.1 K, and using Equation 2 in AG, we find that  $T_{ex} \sim 10.5$  K.

The value of  $T_{ex} \sim 10.5$  K should be taken as a lower limit, as other studies have shown gas in most outflows is usually warmer (by a factor of a 1 to 10) than the ambient cloud gas (e.g., Snell, Loren, & Plambeck 1980; Fukui et al. 1993; Bence, Richer, & Padman 1996; Hatchell, Fuller & Ladd 1999; Davis et al. 2000). Our high spatial resolution data taken with the IRAM 30 m telescope (see Paper II) include simultaneous observations of the  $^{12}$ CO(2–1) and  $^{12}$ CO(1–0) lines, at the same position, which can be used in concert to obtain an estimate of  $T_{ex}$  (e.g., Levreault 1988). Our estimates (see Paper II for specifics) indicate that in most places  $10 \lesssim |T_{ex}| \lesssim 15$ , and that there are only very few positions with  $T_{ex} > 30$  K. Changing the excitation temperature from 10.5 K to 15 K, the outflow mass estimate would increase

by a factor of only 1.1. A change in  $T_{ex}$  from 10.5 K to 30 K, increases the outflow mass estimate by a factor of 1.76. Thus, since most of the outflow gas is at temperatures between 10 and 15 K, assuming  $T_{ex} = 10.5$  K does not lead to a significant uncertainty in the outflow mass estimate.

### 3.4.2. Mass-Velocity Relation

Outflows usually show a mass-velocity relation (mass spectrum) in which  $dM(v)/dv \propto v^{-\gamma}$ , and  $\gamma$  may differ for "high" and "low" velocities in the flow (see Arce & Goodman 2001a). Using the method described above, we calculate the mass per 0.22 km s<sup>-1</sup>wide velocity channel in the redshifted and blueshifted lobes of the HH 315 molecular outflow. The southern lobe redshifted gas mass as a function of outflow velocity is shown in Figure 7e. The outflow velocity  $(v_{out})$  is defined as the observed velocity (v) minus the "ambient" molecular cloud velocity in the redshifted lobe region ( $v_{amb,south} = 2.50 \text{ km s}^{-1}$ , see §3.3 and Table 1). We confidently detect redshifted outflow emission at outflow velocities between 0.71 and 3.79 km s<sup>-1</sup> (that is, from the 0.22 km s<sup>-1</sup>-wide channel centered at outflow velocity  $0.82 \text{ km s}^{-1}$  to the channel centered at  $v_{out} = 3.68 \text{ km s}^{-1}$ ). At outflow velocities lower than 0.71 km s<sup>-1</sup> the structure of the molecular gas (both <sup>12</sup>CO and <sup>13</sup>CO) is nothing like the structure of the higher velocity outflowing gas, and resembles the PV Ceph cloud structure. Therefore, we are confident that all of the molecular gas at  $v_{out} > 0.71 \text{ km s}^{-1}$  is outflow emission. The upper value of the redshifted velocity ( $v_{out} = 3.68 \text{ km s}^{-1}$ ) is constrained by the sensitivity of our observations. Figure 7e shows that the observed mass (per 0.22 km s<sup>-1</sup>wide velocity channel) has a single power-law dependence on velocity for the range of outflow velocities in which we detect redshifted outflow emission. A power-law fit yields a slope of  $-3.4 \pm 0.2$ . We estimate a total redshifted outflow mass, within the box shown in Figure 6, in the velocity range  $0.71 < v_{out} < 3.79 \text{ km s}^{-1}$ , of  $1.8 \text{ M}_{\odot}$ .

The northern lobe blueshifted gas mass as a function of outflow velocity is shown in Figure 7f. We detect blueshifted outflow emission at outflow velocities between -0.71 and -4.45 km s<sup>-1</sup>. Similar to the southern lobe region, outflow velocities in the northern region are defined as the observed velocity minus the "ambient" central velocity. In the northern outflow region the ambient velocity is  $v_{LSR,north} = 1.5$  km s<sup>-1</sup> (see §3.3 and Table 1). At outflow velocities slower than -0.71 km s<sup>-1</sup> the structure of the <sup>12</sup>CO starts to be much more extended than the <sup>12</sup>CO bow-shock like structure seen at faster outflow velocities, and thus we do not include any emission at  $v_{out}$  slower than -0.71 km s<sup>-1</sup> in our blue lobe mass estimate. The CO data we use in this paper show low level blueshifted outflow emission at  $|v_{out}| > 4.45$  km s<sup>-1</sup>, but not at high enough signal-to-noise levels to study it. The higher

resolution data in Paper II show the high velocity structure of the CO outflow clearly, and we discuss its importance there. Figure 7e shows that the observed mass per 0.22 km s<sup>-1</sup>-wide velocity channel (or mass spectrum) has a power-law dependence on outflow velocity for  $0.8 \lesssim |v_{out}| \lesssim 1.5$  km s<sup>-1</sup>, with a slope of  $-2.2 \pm 0.1$ , and for the velocity range of  $1.5 \lesssim |v_{out}| \lesssim 4.2$  km s<sup>-1</sup>, the mass spectrum has slope of  $-3.7 \pm 0.1$ . We obtain a total blueshifted outflow mass in the velocity range  $-4.45 < v_{out} < -0.71$  km s<sup>-1</sup>, within the box shown in Figure 6, of  $4.1 \text{ M}_{\odot}$ .

The blueshifted molecular outflow lobe of HH 315 has a  $\gamma = 2.2 \pm 0.1$  for velocities  $-1.59 < v_{out} < -0.71$  km s<sup>-1</sup> (see Figure 7f). At this velocity range the only molecular outflow structure observed is the bow shock-like structure coincident with HH 315C. This structure was presumably formed, solely, by the interaction of the HH 315C mass ejection event with the ambient cloud. Thus the value of  $\gamma = 2.2 \pm 0.1$  is consistent with the value predicted for an outflow created by one mass ejection episode (see Arce & Goodman 2001a; Matzner & McKee 1999). The episodic nature of the HH 315 outflow is further discussed in Paper II.

The  $^{12}CO(2-1)$  channel maps (Figure 2,  $v_{chan} = 2.98, 3.63 \text{ km s}^{-1}$ ) show that there is localized redshifted emission in the same region of the main blueshifted outflow lobe (near HH 315C). We mentioned earlier (§3.1) that it is likely that this redshifted emission comes from gas that has been accelerated by the "back side" of the HH 315C bow shock. Therefore, it should also be considered as outflow emission, and should be included in the mass and energy estimates of the outflow. Hereafter we refer to the blueshifted and redshifted outflow emission north of PV Ceph as the northern lobe. In Figure 6 we indicate the region used to calculate the mass of the northern lobe redshifted emission. The average <sup>12</sup>CO(1-0) and <sup>13</sup>CO(1–0) spectra in this region (see Figure 8) indicate that the ratio of these two lines  $(R_{12/13})$  is approximately constant in the velocity range where there is redshifted outflow emission (2.55 < v < 3.65 km s<sup>-1</sup>), with an average line ratio ( $\bar{R}_{12/13}$ ) of 10. We therefore estimate the redshifted outflow mass in the north lobe using the same method described above, but instead of assuming a velocity-dependent  ${}^{12}CO(1-0)$  line opacity, we assume that the opacity is constant with  $\bar{R}_{12/13} = 10$ . The resultant molecular outflow mass of the northern lobe redshifted emission over the outflow velocity range  $1.05 < v_{out} < 2.15$ , in the area shown in Figure 6, is  $0.7 \text{ M}_{\odot}$ .

Unlike AG (where we study the HH 300 outflow), we do not subtract for the ambient cloud emission contribution to the outflow emission at low outflow velocities (see §3.3.3). In the case of the HH 315 molecular outflow there is no indication that at the chosen outflow velocities there is "contamination" from the ambient cloud emission. As discussed above, the molecular gas emission (at the velocities used for calculating the outflow mass) has a

structure very different from that of the ambient cloud and a structure which is consistent with that of an outflow lobe. Thus, we are confident that we *do not* need to correct our HH 315 CO outflow mass estimate by the "contamination" of ambient cloud emission.

#### 4. Discussion

#### 4.1. Mass and Energetics of the Outflow

#### 4.1.1. The southern lobe

The total mass of the southern (redshifted) lobe is 1.8  $M_{\odot}$ . The mass of the PV Ceph cloud (as defined in §3.2, also see Figure 5) is about 74  $M_{\odot}$ . Hence, the detectable redshifted outflow lobe mass is only  $\sim 2\%$  of the PV Ceph cloud mass. The mass of the PV Ceph cloud in the redshifted lobe area (as defined in Figure 6) is 29  $M_{\odot}$ . Even in this localized area, the detectable redshifted outflowing mass is only about 4% of the cloud mass. The measured (line-of-sight) momentum  $(\Sigma m(v_i)v_i)$  of the redshifted outflow lobe, for 0.71 <  $v_{out} < 3.79 \text{ km s}^{-1}$ , is  $2.1 \text{ M}_{\odot} \text{ km s}^{-1}$ . The true momentum in the redshifted outflow lobe should be substantially more, as we have only considered the line-of-sight velocity component. If we assume that the angle, i, between the plane of the sky and the outflow's "average" axis is about 10° (GKW), then the outflow momentum would be about 12.1  $M_{\odot}$  km s<sup>-1</sup>. Our ignorance of the exact value of i brings large uncertainties to the value of the outflow momentum. For example, a change in the value of i from  $10^{\circ}$  to  $15^{\circ}$  changes the value of the red lobe momentum from 12 to 8  $M_{\odot}$  km s<sup>-1</sup>. The kinetic energy is even more uncertain, as it depends on  $(\sin i)^{-2}$ . We estimate the kinetic energy  $[(\frac{1}{2}) \Sigma m(v_i)v_i^2]$  of the red lobe, for  $0.71 < v_{out} < 3.79 \text{ km s}^{-1}$ , to be  $2.9 (\sin i)^{-2} \times 10^{43} \text{ erg}$ . Using  $i = 10^{\circ}$ , the kinetic energy is then  $9.6 \times 10^{44}$  erg.

# 4.1.2. The northern lobe

The mass of the blueshifted gas at the outflow velocity range  $-4.45 < v_{out} < -0.71 \,\mathrm{km \, s^{-1}}$  in the north lobe of the PV Ceph molecular outflow is  $4.1 \,\mathrm{M_{\odot}}$ . If we include the  $0.7 \,\mathrm{M_{\odot}}$  of outflowing redshifted emission (at  $1.05 < v_{out} < 2.15 \,\mathrm{km \, s^{-1}}$ ) detected near the HH 315C optical knot, then the total mass of the northern outflow lobe is  $4.8 \,\mathrm{M_{\odot}}$ . We estimate the mass of the Northern Cloud (see §3.3), from the <sup>13</sup>CO emission, to be 13.5  $\,\mathrm{M_{\odot}}$ . Comparing this amount of mass, with the total northern lobe mass, we see that the outflowing mass in the north region is about one third of what one would naively consider the "ambient" cloud

mass. Later, we show that about half of the mass of the medium-density gas which we at first naively define as the ambient north cloud gas, is in fact gas that has been accelerated by the HH 315 flow (see §4.2.2).

We obtain a line-of-sight momentum of  $5.1~\rm M_{\odot}~km~s^{-1}$  for the blueshifted outflow emission and a line-of-sight momentum of  $1.0~\rm M_{\odot}~km~s^{-1}$  for the redshifted outflow emission in the north lobe, for a sum of  $6.1~\rm M_{\odot}~km~s^{-1}$ . Assuming  $i=10^{\circ}$ , then we obtain a total north lobe momentum of  $35.1~\rm M_{\odot}~km~s^{-1}$ . The kinetic energy estimates for the north lobe are  $7.6~(\sin i)^{-2}\times 10^{43}$  erg for the blueshifted gas and  $1.5~(\sin i)^{-2}\times 10^{43}$  erg for the redshifted gas. If we assume  $i=10^{\circ}$ , then the total kinetic energy of the north lobe is  $3.0\times 10^{45}$  erg. The mass, momentum, and kinetic energy estimates of the HH 315 outflow are listed in Table 2.

### 4.2. The effects of the outflow on the ambient gas

### 4.2.1. The southern lobe and the PV Ceph Cloud

As shown in Figure 5, the projected overlap between outflowing gas and the PV Ceph cloud (as defined in Table 1) is quite small. Nonetheless, it is still interesting to consider what effect(s) the outflow may have on the overall evolution of the PV Ceph cloud. Since the large-scale <sup>12</sup>CO velocity maps in this paper (Figure 2) show no blueshifted outflow lobe emission superimposed on the PV Ceph cloud we only consider the effects of the redshifted lobe in estimating the effects of the HH 315 flow on the dense portion of the star-forming cloud. Note, though, that our higher resolution observations (Paper II) do detect a small amount of blueshifted outflow emission just north of PV Ceph.

One method to quantitatively study the effects of an outflow on its parent cloud is to compare the outflow's energy with the cloud's binding energy. The cloud's binding energy is given by  $E_{grav} \sim GM_c^2/R_c$ , where we estimate  $R_c$  to be the geometric mean of the short and long axes of the PV Ceph cloud ( $\sim 0.7~\rm pc$ ), and  $M_c$ , the mass of the cloud, is  $\sim 74~\rm M_{\odot}$ . Using these values we obtain that the cloud's binding energy is about  $6.7 \times 10^{44}~\rm erg$ . If the HH 315 flow has an inclination to the plane of the sky of  $i \sim 10^{\circ}$ , then the southern lobe of HH 315 has enough kinetic energy ( $9.6 \times 10^{44}~\rm erg$ ) to gravitationally unbind its parent cloud—if that energy is efficiently coupled to the cloud (see below). Given the substantial amount of kinetic energy in the southern lobe, the flow might be able to disperse a major fraction of the very dense gas, where most of the binding mass is located. This in turn would alter the gravitational potential well of the cloud.

We may indeed already be seeing the start of the PV Ceph cloud's disruption by the

HH 315 flow. In Figure 9a we plot, in contours, the integrated intensity of the HH 315 molecular outflow's south lobe, superimposed on the  $^{13}$ CO integrated intensity over the velocity range  $1.84 < v < 2.17 \text{ km s}^{-1}$ . It can be seen that the molecular outflow's southern lobe fits in the  $^{13}$ CO cavity seen just south of PV Ceph. This spatial coincidence suggests that the cavity was formed by the the outflow-cloud interaction. In addition, the peak  $^{13}$ CO integrated intensity over the velocity range  $2.17 < v < 2.61 \text{ km s}^{-1}$  borders the southern lobe's position (see Figure 9b). This structure in the  $^{13}$ CO also suggests that the southern lobe has pushed and redistributed the medium-density ambient gas.

In order to further investigate the hypothesis that the southern molecular outflow lobe is responsible for the minimum in the  $^{13}$ CO distribution observed south of PV Ceph, we studied the velocity distribution of the  $^{13}$ CO in the region (see spectrum in Figure 10). We made an average of the  $^{13}$ CO emission in the cavity and fit it with a two-Gaussian function (the small blueshifted velocity component is due to cloud X). The fit yields a central velocity of 2.6 km s<sup>-1</sup> for the velocity component associated with the PV Ceph cloud. This is only 0.1 km s<sup>-1</sup> larger than  $v_{amb,south}$ . Even though the difference is small, it is still significant as the 1- $\sigma$  error in the central velocity fit is about 0.01 km s<sup>-1</sup>.

In Figure 11 we show (in white contours) a  $^{12}\text{CO}(2\text{--}1)$  position-velocity (p-v) diagram superimposed on a grey-scale  $^{13}\text{CO}(1\text{--}0)$  p-v diagram. Both p-v diagrams are constructed by summing all spectra over the width of the  $^{13}\text{CO}$  cavity seen in Figure 9a. The cavity is seen as a minimum in the  $^{13}\text{CO}$  emission at velocities between  $\sim 1.5$  and  $\sim 2.2$  km s<sup>-1</sup>, at 0 to 2.5' offset from the position of PV Ceph. This minimum in the  $^{13}\text{CO}$  emission (or cavity) is bordered to the north and south by emission from the PV Ceph cloud. The redshifted "border" of the cavity is formed by the emission of the PV Ceph cloud and the blueshifted border is defined by emission from Cloud X. At the same position of the cavity there is a notch in the  $^{12}\text{CO}(2\text{--}1)$  p-v diagram. This notch indicates that there is also a minimum in the  $^{12}\text{CO}(2\text{--}1)$  emission at the position and velocity of the  $^{13}\text{CO}$  cavity, and that there is a bulk shift in the velocity distribution of the  $^{12}\text{CO}(2\text{--}1)$  gas towards redshifted velocities.

One possible scenario which fits the data is that the south molecular (redshifted) lobe pushed and accelerated the ambient cloud gas. The cavity can only be seen at low blueshifted velocities (relative to the PV Ceph cloud's central velocity,  $v_{LSR,south} = 2.50 \text{ km s}^{-1}$ ) since the redshifted outflow lobe has only been able to slightly change the velocity distribution (toward redshifted velocities) of the dense gas it has interacted with, and it yet has to clear the region completely. If the outflow does not turn off, then given more time, more ambient gas will be shoved away and accelerated, making the cavity larger and visible at all velocities.

We may also value the role of the HH 315 flow in the PV Ceph cloud by comparing the southern lobe's kinetic energy with the cloud's turbulent kinetic energy. The total kinetic energy of a cloud where thermal motions are a negligible part of  $\Delta V$  (the observed FWHM velocity line width), is given by  $E_{turb} = \frac{3}{16 \ln 2} M_c \Delta V^2$ , where  $M_c$  is the cloud mass. The average <sup>13</sup>CO velocity width in the PV Ceph cloud is  $\Delta V \sim 0.6$  km s<sup>-1</sup>, so  $E_{turb} \sim 1.2 \times 10^{44}$  erg. The outflow kinetic energy is about 2.9 (sin i)<sup>-2</sup> × 10<sup>43</sup> erg in the southern lobe, thus, even if  $i = 29^{\circ}$ , the southern lobe kinetic energy exceeds the cloud's turbulent kinetic energy. Similar to what is observed in the giant molecular outflow HH 300 (AG), the southern lobe of the HH 315 molecular outflow has enough kinetic energy to potentially feed the turbulence in its parent cloud.

Another way to estimate the impact of the HH 315 outflow on the PV Ceph cloud is by comparing the outflow's energy with the chemical binding energy of the molecules in the cloud. If we assume  $i=10^{\circ}$ , then the kinetic energy of the molecular outflow is about  $9.6\times10^{44}$  erg. This energy would be enough to dissociate about  $10^{53}$  H<sub>2</sub> molecules (each with a molecular binding energy of 4.5 eV). This amount of molecules is equivalent to 0.2 M<sub> $\odot$ </sub>, which is only a mere 0.3% of the total mass of the cloud. Therefore, the potential disruption of molecules by the HH 315 flow will have no significant impact on the PV Ceph cloud as a whole.

Yet another way to asses the importance of the HH 315 outflow energy input on its parent cloud is by comparing the flow's power with the power needed to maintain the magnetohydrodynamic (MHD) turbulence in the PV Ceph cloud. The three-dimensional numerical simulations of Stone, Ostriker, & Gammie (1998) and Mac Low (1999) study MHD turbulence under density, temperature and magnetic field conditions representative of those found in Galactic molecular clouds. Using Equation 7 in Mac Low (1999), we can estimate the input power needed to maintain MHD turbulence in the PV Ceph cloud (shown in Figure 5). We use the estimated mass of the PV Ceph cloud (74  $\rm M_{\odot}$ ) and the average velocity line width of the  $^{13}\rm CO$  (0.6 km s<sup>-1</sup>). Using these values we find that about 0.01  $\rm L_{\odot}$  of input power at a scale of 0.5 pc (the approximate length of the southern lobe) are needed to counter the dissipation of MHD turbulence in the PV Ceph cloud.

The power of an outflow is usually estimated by dividing the outflow kinetic energy by the dynamical age of the outflow. The conventional way to estimate the dynamical age of a molecular outflow assumes that all the gas in the outflow originates at the young star. This assumption is wrong, since the vast majority of the gas in a molecular outflow comes from the entrained gas in the host cloud (along the extent of the outflow) that has been put in motion by the underlying stellar wind. Since there is no way to obtain an accurate estimate of the outflow lifetime, we estimate a lower and an upper bound to the dynamical age in order to estimate an upper and lower bound to the outflow power. We estimate the lower limit to be the time it has taken HH 315F (the HH knot which currently lies farthest

from the source) to travel to its current position. The distance from PV Ceph to HH 315F is 1.41 pc (RBD), and if we assume a tangential velocity of 200 km s<sup>-1</sup>, we then obtain a dynamical age of about 6900 yr. As an upper limit on the age we use  $2 \times 10^5$  years, the statistical lifetime of outflows as derived by the study of Parker, Padman, & Scott (1991). We then estimate the lower and upper limits of the outflow power to be  $1.2 \times 10^{-3}$  (sin i)<sup>-2</sup> to  $3.4 \times 10^{-2}$  (sin i)<sup>-2</sup> L<sub> $\odot$ </sub>. If we assume that  $i \sim 10^{\circ}$ , then the southern lobe's power is more than the estimated power needed to maintain the MHD turbulence in the PV Ceph cloud.

Note that we only compare the outflow power to that needed to sustain the MHD turbulence and stop gravitational collapse in the cloud, to quantify the possible effect that outflows have on their parent cloud: by no means we are implying that molecular clouds need to be maintained in gravitational equilibrium. Our results for HH 315 (this paper) and HH 300 (AG) imply that outflows are sources of non-negligible power in clouds, and they should be treated as such in numerical simulations of MHD turbulence in star-forming clouds.

The energy in the HH 315 outflow southern lobe is comparable or larger than the binding energy, and the turbulent energy, of the PV Ceph cloud. But, this does not necessarily mean that the outflow will be able to unbind the cloud or turn all its energy into cloud turbulent energy. We would be able to make a rough prediction of the PV Ceph cloud's future from our observations, if we knew how well the outflow energy couples to the cloud. The <sup>13</sup>CO cavity coincident with the southern outflow lobe, the <sup>13</sup>CO shell structure in the north, coincident with the outer edge of the northern blueshifted lobe, and the velocity gradient in the velocity of the ambient gas (see below) are all examples that there is some degree of coupling between the outflow and the ambient gas. Just from observational data, though, it is very hard to predict the outflow-cloud coupling efficiency of any outflow. No sufficiently good episodic outflow-cloud interaction model exists (see Arce & Goodman 2001a). There is a need for theoretical and numerical studies which concentrate on studying how efficiently can bulk motions, produced by outflows, unbind a cloud and/or produce turbulence, as a function of cloud density and outflow energy.

# 4.2.2. The northern lobe and the Northern Cloud

The northern lobe of the PV Ceph molecular outflow is characterized by its bow shocklike structure, coincident with the optical knot HH 315C, most evident at low outflow velocities (see Figure 2). A shell-like structure, surrounding the blueshifted outflow lobe, can be seen in  $^{13}$ CO emission at very low (between 0.79 and 1.45 km s<sup>-1</sup>) velocities (see Figures 3a and 12). Most of the northern lobe region is essentially devoid of  $^{13}$ CO emission, and the majority of the <sup>13</sup>CO emission present in the region surrounds the western and northern edge of the <sup>12</sup>CO bow shock structure (see Figure 12). It appears that the HH 315 flow has been able to push gas north of PV Ceph, piling it in a dense shell-like structure surrounding the outflow lobe, which we detect in <sup>13</sup>CO(1–0).

Using the  $^{13}$ CO emission surrounding the blueshifted lobe at velocities between 0.79 and 1.45 km s<sup>-1</sup>, we estimate the shell structure's mass to be 6.8 M<sub> $\odot$ </sub> and momentum to be 2.5 M<sub> $\odot$ </sub> km s<sup>-1</sup>. The line-of-sight momentum of the shell is sightly smaller than the line-of-sight momentum of the blueshifted outflow emission (which is equal to 5.1 M<sub> $\odot$ </sub> km s<sup>-1</sup>). The morphology of the shell-like structure (which surrounds the blueshifted outflow lobe), its slow blueshifted velocity, and the fact that its momentum is at least similar to the blueshifted outflow momentum are all consistent with the  $^{13}$ CO shell having been formed by the HH 315's (momentum-conserving) entrainment of the ambient molecular gas.

The velocities at which the  $^{13}$ CO shell structure is seen fall inside the range of velocities which we defined earlier (§§3.3 and 4.1.2) as the north cloud ambient cloud. Thus, in fact we see that a substantial fraction (6.8/13.5  $\sim 50\%$ ) of what we had earlier naively defined as "Northern Cloud ambient gas" in reality is medium density gas that has been accelerated by the outflow. In fact, the peak  $^{13}$ CO emission shell structure can be nicely seen in the  $^{13}$ CO p-v diagram (Figure 4), at about 6′ ( $\sim 0.75$  pc) from the source (along the P.A.=-26° axis), at a velocity of about 1.35 km s<sup>-1</sup>. Thus, most of the cloud structure in the northern lobe region, as defined by the  $^{13}$ CO emission, comes from gas that has been greatly affected by the outflow. One might say that in this region "the cloud is the outflow and the outflow is the cloud".

In Figure 13 we plot the  $^{12}\text{CO}(2-1)$  position-velocity (p-v) diagram of the mapped region, constructed by summing all spectra along an axis with a position angle of -26°. By summing the  $^{12}\text{CO}(2-1)$  spectra over a limited width (see Figure 6) of the  $^{12}\text{CO}(2-1)$  map, we avoided including most (but not all) of the region where cloud X lies, so that its emission would not "contaminate" the  $^{12}\text{CO}(2-1)$  p-v diagram. The main features of the  $^{12}\text{CO}(2-1)$  p-v diagram are the peaks in the maximum velocity associated with the blueshifted (north) and redshifted (south) lobes. A local increase in the maximum velocity may be seen at the position (along the average axis) of the optical HH knots A, B, C, and D, and close to the position of PV Ceph. The velocity structure at the position of each of these optical knots is characteristic of the bow shock (prompt) entrainment mechanism, which will produce the highest velocities at the head of the shock (the position of the HH knot) and decreasing velocity trend towards the source (e.g., Bence et al. 1996; Lee et al. 2000; 2001). The fact that we see several of these velocity increases (or bumps) in the p-v diagram, and each is coincident with a different HH knot is also evidence that HH 315 flow is an episodic outflow

(see Arce & Goodman 2001a). The increase in redshifted velocities at about -1' offset from the source position is mainly due to the redshifted outflow lobe. We further discuss this velocity feature, and the kinematics of HH 315 molecular outflow in Paper II.

In addition to the kinematical structure associated with the HH knots, the north half of the p-v diagram shows evidence for a velocity gradient in the ambient gas' central velocity  $(v_{LSR})$ . The ambient cloud's  $v_{LSR}$  may be approximated as the velocity where the peak contour, in the p-v diagram, lies. In the  $^{12}\text{CO}(2-1)$  p-v diagram, the peak contour is seen to shift from about 2.5 km s<sup>-1</sup> at the position of PV Ceph down to about 1.5 km s<sup>-1</sup> near HH 315A. We believe that the northern lobe of the HH 315 outflow is responsible for the gradient in the central velocity of the ambient cloud. In addition, the fact that more than half of the gas mass in the northern region has been accelerated by the outflow gives additional support to our hypothesis.

In any volume of momentum-conserving wind-cloud interaction high-density gas will be accelerated less than gas at low densities. This is what we observe in the ambient gas surrounding HH 315. The ambient gas north of PV Ceph (where we detect an obvious velocity gradient) is much less dense than the ambient gas to the south (where we cannot easily detect a large-scale velocity gradient in the CO emission). The ambient density contrast between north and south of PV Ceph is clear from our <sup>13</sup>CO integrated intensity map (Figure 5) and from the relative extinction measurements between the region around HH 315B and HH 315D (GKW). We may also estimate the density contrast, from the ambient gas velocity gradient in each region. We assume that the velocity gradient in the ambient gas central velocity  $(\Delta v_a)$  is wholly due to the momentum conserving stellar wind-ambient gas interaction, and that the stellar wind deposits all its momentum  $(\rho_w v_w)$  on the ambient gas, so that  $\rho_w v_w \approx \rho_a \Delta v_a$ . We assume that the wind momentum of each lobe is the same. The  $^{12}\mathrm{CO}(2-1)$  shows a velocity gradient to the north of  $\sim 1~\mathrm{km~s^{-1}}$  (see Figure 13). The  $^{12}$ CO(2-1) p-v diagram shows no velocity gradient in the ambient gas south of PV Ceph due to the coarse velocity resolution (0.65 km  $\rm s^{-1}$ ) of the  $^{12}CO(2-1)$  data. However, the  $^{13}\mathrm{CO}$  data shows a velocity shift of  $\sim 0.1~\mathrm{km~s^{-1}}$  in the southern molecular outflow lobe region (see §4.2.1, and Figure 10). Thus, we estimate that the ambient gas density south of PV Ceph is about a factor of 10 larger than the ambient gas density north of PV Ceph.

# 5. Summary and Conclusion

We mapped the giant molecular outflow associated with the HH 315 flow, from the star PV Cephei, in the  $^{12}CO(2-1)$  line, with a beam size of 27". We also made more extended maps of the gas surrounding the HH 315 flow in the  $^{12}CO(1-0)$  and  $^{13}CO(1-0)$  lines, with

45'' and 47'' beam sizes, respectively. By observing a large extent of the gas surrounding the outflow we are able to study the outflow in the context of its surrounding medium. Also, the  $^{13}$ CO observations help us assess the effects the outflow has on the surrounding moderate-density ( $n \sim 10^3 \text{ cm}^{-3}$ ) gas structure and kinematics. In addition, the combined  $^{12}$ CO(1–0) and  $^{13}$ CO(1–0) line observations enable us to estimate the mass of the outflow by correcting for the velocity-dependent opacity of the  $^{12}$ CO(1–0) line.

The outflow source, PV Ceph, is a young star forming in the northern edge of its dark cloud. Hence, the northern and southern lobes of the HH 315 outflow are interacting with environments with drastically different densities. The southern lobe has a mass of 1.8  $M_{\odot}$ and interacts with the dense region we define as the PV Ceph cloud. We quantify the effects that the HH 315 flow has on the PV Ceph cloud by using different methods. Assuming that HH 315 has an inclination to the plane of the sky (i) of about 10°, then the southern lobe of the HH 315 molecular outflow has a momentum of 12.1  $M_{\odot}$  km s<sup>-1</sup> and a kinetic energy of  $9.6 \times 10^{44}$  erg. The kinetic energy of the southern outflow lobe is enough to supply the turbulent energy of the PV Ceph cloud  $(1.2 \times 10^{44} \text{ erg})$ , and enough energy to gravitationally unbind it (the gravitational binding energy of the PV Ceph cloud is  $\sim 6.7 \times 10^{44}$  erg). We compare our estimate of the southern lobe's mechanical power, with that of the power needed to sustain the MHD turbulence in the PV Ceph cloud (using the results of the numerical models of Stone, Ostriker, & Gammie 1998 and Mac Low 1999). If we assume that  $i \sim 10^{\circ}$ , then the southern lobe's power is more than the estimated power needed to maintain the MHD turbulence in the PV Ceph cloud. In addition, the <sup>13</sup>CO data indicate that the southern HH 315 flow is having a major effect on the distribution of the ambient cloud gas. We detect a cavity in the distribution of the <sup>13</sup>CO in the PV Ceph cloud region. The <sup>13</sup>CO gas velocity and density distribution, and the morphology of the outflowing <sup>12</sup>CO(2–1) gas suggests that the cavity has been formed by the southern outflow lobe interaction with its surroundings.

The northern (mostly blueshifted) lobe has a total mass of 4.8  $M_{\odot}$  and interacts with an environment which is much less dense (by about a factor of ten) than the environment south of PV Ceph. There is much less <sup>13</sup>CO emission north of PV Ceph, and most of the <sup>13</sup>CO emission is concentrated in a shell-like structure about 1.2 pc northwest of PV Ceph, coincident with the outer edge of northern outflow lobe. It appears that the northern lobe of the HH 315 molecular outflow has "pushed" aside the <sup>13</sup>CO, piling the gas in a shell-like structure at its edges. The morphology of the shell-like structure, its slow blueshifted velocity, and the fact that its momentum is very similar to the blueshifted outflow lobe momentum are all consistent with the shell being formed by the (momentum-conserving) entrainment of the ambient molecular gas in the HH 315 flow. Adding the mass in the northern molecular outflow, and the mass of the <sup>13</sup>CO shell, we find that more than 50% of

the total gas mass in the region of the northern outflow lobe has been put into motion by the outflow. The northern outflow lobe of HH 315 is having a major impact on the structure of the ambient medium, even at a distance of about 1 to 1.4 pc from the outflow source.

In addition, we detect a velocity gradient in the ambient cloud's central velocity north of PV Ceph. The gradient is towards blueshifted velocities, in the same sense as the vast majority of the outflowing gas in the northern outflow lobe. We argue that the gradient in the cloud's central velocity is due to the HH 315 outflow, as the gradient is consistent with it being formed by a momentum-conserving outflow-cloud interaction. The fact that the outflowing gas mass north of PV Ceph is a major fraction of the total gas mass, supports our picture in which the HH 315 flow is responsible for the velocity gradient in the ambient gas north of PV Ceph.

Our study clearly shows that the HH 315 flow is effecting the kinematics of its surrounding medium, and has been able to redistribute considerable amounts of its surrounding medium-density ( $\sim 10^3 \ {\rm cm}^{-3}$ ) gas in its star-forming core as well at parsec-scale distances from the source. These are necessary steps in the clearing of the gas surrounding a forming star and the eventual (total) disruption of the parent cloud. We conclude that the giant outflow from PV Ceph is having a profound effect on its host cloud's evolution and fate. It is tempting to generalize this result, along others like it, and suggest that outflows have great influence on the sculpting of star-forming molecular clouds.

We would like thank Paul Ho, and Charlie Lada for their helpful comments on this work. We would also like to thank Bo Reipurth for his comments and the optical image of PV Ceph. And we are grateful to the National Science Foundation for supporting this effort through grants AST 94-57456 and AST 97-21455.

#### REFERENCES

Arce, H. G., & Goodman, A. A. 2001a, ApJ, 551, L171

Arce, H. G., & Goodman, A. A. 2001b, ApJ, 554, 132 [AG]

Arce, H. G., & Goodman, A. A. 2002, in press [Paper II]

Bally, J., Reipurth, B., Lada, C. J., & Billawala, Y. 1999, AJ, 117, 410

Bence, S. J., Richer, J. S., & Padman, R. 1996, MNRAS, 279, 866

Cabrit, S., & Raga, A. 2000, A&A, 354, 667

Cantó, J., Espresate, J., Raga A. C., & D'Alessio P. 1998, MNRAS, 296, 1041

Cernicharo, J., & Reipurth, B. 1996, ApJ, 460, L57

Cohen, M., Kuhi, L. V., Harlan, E. A., & Spinrad, H. 1981, ApJ, 245, 920

Davis, C. J., Dent, W. R. F., Matthews, H. E., Coulson, I. M., & McCaughrean, M. J. 2000, MNRAS, 318, 952

Davis, C. J., Smith, M. D., Moriarty-Schieven, G. H. 1998, MNRAS, 299, 825

Devine, D. 1997, Ph.D. Thesis, University of Colorado

Devine, D., Bally, J., Reipurth, B., & Heathcote, S. 1997, AJ, 114, 2095

De Young D. S., & Axford W. I. 1967, Nature, 216, 129

Eislöffel, J. 2000, A&A, 354, 236

Eislöffel, J. & Mundt, R. 1997, AJ, 114, 280

Fukui, Y., Iwata, T., Mizuno, A., Bally, J., & Lane, A. 1993, in Protostars & Planets III, ed. E. H. Levy & J. I. Lunine (Tucson: Univ. Arizona Press), 603

Gammie, C. F., & Ostriker, E. C. 1996, ApJ, 466, 814

Gómez, M., Kenyon, S., & Whitney, B. A. 1997, AJ, 114, 265

Goodman, A. A., & Arce, H. G. 2002, in preparation

Heyer, M. H., Vrba, F. J., Snell, R. L., Schloerb, F. P., Strom, S. E., Goldsmith, P. F., & Strom, K. M. 1987, ApJ, 321, 855

Hatchell, J., Fuller, G. A., & Ladd, E. F. 1999, A&A, 344, 687

Kutner, M. L., & Ulich, B. L. 1981, ApJ, 250, 341

Lada, C. J., & Fich, M. 1996, ApJ, 459, 638

Langer, W. D., & Penzias, A. A. 1993, ApJ, 408, 539

Lee, C.-F., Mundy, L. M., Reipurth, B., Ostriker, E. C., & Stone, J. M. 2000, ApJ, 542, 925

Lee, C. F., Stone, J. M., Ostriker, E. C., & Mundy, L. G. 2001, ApJ, 557, 429

Levreault, R. M. 1984, ApJ, 277, 634

Levreault, R. M. 1989, ApJS, 67, 283

Levreault, R. M., & Opal, C. B. 1987, AJ, 93, 669

Mac Low, M.-M. 1999, ApJ, 524, 169

Mader, S. L., Zealey, W. J., Parker, Q. A., & Masheder, M. R. W. 1999, MNRAS, 310, 331

Margulis, M., & Lada, C. J. 1985, ApJ, 299, 925

Masson, C. R., & Chernin, M. L. 1993, ApJ, 414, 230

Neckel, T., Staude, H. J., Sarcander, M., & Birkle, K. 1987, A&A, 175, 231

Norman, C., & Silk, J. 1980, ApJ, 238, 158

Reipurth, B., Bally, J., & Devine, D. 1997, AJ, 114, 2708

Richer, J. S., Hills, R. E., & Padman, R. 1992, MNRAS, 254, 525

Snell, R. L., Loren, R. B., & Plambeck, R. L. 1980, ApJ, 239, L17

Scarrott, S. M., Rolph, C. D., & Tadhunter, C. N. 1991, MNRAS, 249, 131

Stanke, Th., McCaughrean, M. J., & Zinnecker, H. 2000, A&A, 355, 639

Stone, J. M., Ostriker, E. C., & Gammie, C. F. 1998, ApJ, 508, L99

Yu, K. C., Billawala, Y., & Bally, J. 1999, AJ, 118, 2940

This preprint was prepared with the AAS IATEX macros v5.0.

- Fig. 1.— Integrated intensity contour map of the  $^{12}\text{CO}(2\text{--}1)$  HH 315 outflow superimposed on a wide-field  $\text{H}\alpha+[\text{S II}]$  (optical) CCD image from RBD. The blueshifted lobe, which is integrated over the velocity range  $-2.55 < v < 0.7 \text{ km s}^{-1}$ , is represented by the light grey contours. The first contour and contour steps of the blueshifted lobe are 1.04 and 0.52 K km s<sup>-1</sup>, respectively. We cut out the contribution from cloud X (see text) from the integrated intensity map of the blueshifted lobe, hence the cut contours at the westernmost edge of the lobe. The redshifted emission is represented by the dark contours. The redshifted emission in the north lobe is integrated over the velocity range  $2.65 < v < 3.30 \text{ km s}^{-1}$ . The southern redshifted lobe is integrated over the velocity range  $3.30 < v < 6.55 \text{ km s}^{-1}$ . The first contour and contour steps of both north and south redshifted integrated intensity emission all have a value of  $0.52 \text{ K km s}^{-1}$ . The position of the HH knots in the optical map, and the position of PV Ceph are shown. The extent of the OTF map is indicated by the jagged thin line. The FWHM beam of the NRAO 12 m telescope is shown on the bottom-right corner.
- Fig. 2.— Velocity channel maps of the <sup>12</sup>CO(2–1) emission. Each velocity channel is 0.65 km s<sup>-1</sup> wide. The center velocity of the channel is shown on the upper-left corner of each panel. The starting contour and the contour steps are both 0.325 K km s<sup>-1</sup> for all panels. The position of the outflow source (PV Ceph) is represented by the star symbol, at the center of each panel. The crosses show the position of the brightest (optical) point of the different HH knots which make the HH 315 flow, knots C, B, A, D, E, F (from top to bottom) (RBD). We also identify the cloud structure we define as cloud X. The linear scale, assuming a distance to the source of 500 pc, is shown. The FWHM beam of the NRAO 12 m telescope is also shown.
- Fig. 3.— Velocity-range-integrated intensity maps of the  $^{13}$ CO(1–0) emission. The velocity interval of integration is given on the top of each panel. The first contour, which is also the value of the contour steps, is given inside brackets on the bottom-right corner of each panel in units of K km s<sup>-1</sup>. The position of the outflow source, PV Ceph, is identified with a star symbol. The cross symbols indicate the position of the HH knots, the same as in Figure 1. In panel (a) we identify the filamentary structure associated with cloud X. We also indicate the shell-like structure formed by the blueshifted lobe of the HH 315 outflow (see §4.2.2). In panel (c) we show the cavity in the  $^{13}$ CO emission presumably formed by the redshifted (southern) lobe of HH 315 (see §4.2.1).
- Fig. 4.— Position-Velocity (p-v) diagram of the  $^{13}\mathrm{CO}(1\text{--}0)$  emission, constructed by summing all spectra along an axis with a P.A.=-26° (the outflow "average" axis), over the width of the map. The  $^{13}\mathrm{CO}$  p-v digram is obtained from a smoothed cube of our  $^{13}\mathrm{CO}$  data with a velocity resolution of 0.11 km s<sup>-1</sup>, and 11.5" by 11.5" pixels (see §2.2). The

contours are from 4 to 30 K, in steps of 2 K, and from 35 to 90 K in steps of 5 K. The dashed square on the bottom denotes the limits of our definition of the PV Ceph cloud (see §3.3). The dashed square on the top denotes the limits of what we define in the text as the Northern Cloud (see §3.3). The vertical lines at the top and bottom denote the velocity range of integration of the <sup>13</sup>CO velocity maps shown in Figure 3. The letter at the center of each velocity range indicates the panel in Figure 3 which corresponds to the given range.

Fig. 5.— Integrated intensity grey-scale map of the  $^{13}\text{CO}(1\text{--}0)$  PV Ceph cloud. The velocity range of integration is 1.8 < v < 3.2 km s<sup>-1</sup>. The dashed square denotes our definition of the PV Ceph cloud area (see §3.3). The white contours represent the  $^{12}\text{CO}(2\text{--}1)$  integrated intensity of the redshifted outflow lobe. The contours are the same as in Figure 1, except that here, we only show the  $0.52 \times (1, 2, 4, 6, 8, 10)$  K km s<sup>-1</sup> contours.

Fig. 6.— Map showing different regions defined in the text. The contours are the same as the contours in Figure 1. The dashed square around the blueshifted (northern) lobe and around the southern (redshifted) lobe indicate the region used to obtain the average  $^{12}CO(1-0)$  and  $^{13}CO(1-0)$  spectra shown in Figure 7. The solid square around the blueshifted lobe and around the southern lobe indicate the region used to obtain the outflow mass of each lobe. The solid square around the redshifted emission in the *northern* lobe indicates the region used to obtain the average  $^{12}CO(1-0)$  and  $^{13}CO(1-0)$  spectra shown in Figure 8, and the mass of the northern redshifted outflow emission. The solid grey tilted rectangle shows the area used to obtain the  $^{12}CO(2-1)$  position-velocity diagram of Figure 13.

Fig. 7.— (a) Average spectra over the redshifted (southern) lobe region indicated in Figure 6. Dark line indicates the  $^{13}CO(1-0)$  average spectrum, the light line indicates the  $^{12}CO(1-0)$ average spectrum. (b) The same as [a], but for the blueshifted (northern) lobe. (c) Main beam temperature (or intensity) ratio of <sup>12</sup>CO(1-0) to <sup>13</sup>CO(1-0), using the average spectra in the above panel, as a function of observed velocity (v). This ratio is denoted in the text as  $R_{12/13}$ . The filled circle symbols are the points used for the second-order polynomial fit to  $R_{12/13}$ . The solid line is the resulting fit. (d) The same as [c], but for the blueshifted lobe. (e) Mass spectrum, or mass in a 0.22 km s<sup>-1</sup>-wide channel as a function of outflow velocity  $(v_{out} = v - v_{amb})$ , for the red (southern) lobe of the HH 315 molecular outflow. The filled diamonds represent the outflow, and the unfilled diamonds represent the ambient cloud. The solid line shows a power-law fit to the filled diamonds. The slope of the fit is  $-3.4 \pm 0.2$ . (f) Similar to [e], but for the northern lobe. The dark diamond symbols represent the blueshifted emission. The grey squares represent the redshifted emission in the northern lobe. We made two power-law fits to the blueshifted emission in the northern lobe. The slopes of the fits are  $-2.2\pm0.1$  for the low-outflow velocity range and  $-3.7\pm0.1$  for the high-outflow velocity range. The grey line shows a power-law fit to the northern lobe redshifted outflow emission.

The slope to this fit is  $3.1 \pm 0.8$ .

Fig. 8.— (a) Average spectra over the northern redshifted outflow emission region indicated in Figure 6. Dark line indicates the  $^{13}CO(1-0)$  average spectrum, the light line indicates the  $^{12}CO(1-0)$  average spectrum. (b) Main beam temperature (or intensity) ratio of  $^{12}CO(1-0)$  to  $^{13}CO(1-0)$  —also denoted in the text as  $R_{12/13}$ — as a function of observed velocity (v), using the average spectra in [a].

Fig. 9.— (a) Same grey scale map as in Figure 3c, but with different grey scale range. In addition, we superimpose the integrated intensity contours (white lines) of the  $^{12}$ CO(2–1) southern lobe shown in Figure 1. Notice that the integrated intensity contours of the southern lobe fit well in the  $^{13}$ CO "cavity" (or minimum). (b) Grey scale map similar to Figure 3d. In addition, we superimpose the integrated intensity contours (white lines) of the  $^{12}$ CO(2–1) southern lobe shown in Figure 1. Notice that the maximum  $^{13}$ CO emission borders the western edge of the molecular outflow lobe.

Fig. 10.— Average  $^{13}$ CO(1–0) spectrum over the  $^{13}$ CO cavity south of PV Ceph. The area is indicated by a dashed box in panel Fig. 9b].

Fig. 11.—  $^{12}$ CO(2–1) position-velocity diagram (white contours) superimposed on a  $^{13}$ CO grey-scale position-velocity diagram. Both p-v diagrams are constructed by summing all spectra over the width of the  $^{13}$ CO cavity seen in Figure 9a. The contours in the  $^{12}$ CO(2–1) p-v diagram are 4 to 30 K, in steps of 2 K. The contours in the  $^{13}$ CO(1–0) p-v diagram are 2, 3, 5, 7, 9, 11, 13, 15, 17, 19, 21 K. The box encloses the region of the  $^{13}$ CO p-v diagram shown in more detail in the bottom panel. Several velocity features are identified.

Fig. 12.— Grey scale map similar to Figure 3a. In addition we superimpose the  $^{12}\text{CO}(2-1)$  integrated intensity contours (white lines) of the blueshifted (northern) outflow lobe. Notice the shell-like structure in the  $^{13}\text{CO}$  surrounding the outer edge of the  $^{12}\text{CO}(2-1)$  outflow lobe. The  $^{13}\text{CO}(1-0)$  spectrum shown is an average over the area inside the white dashed box. The spectrum axes have a velocity range of -5 < v < 8 km s<sup>-1</sup> and a main beam temperature range of  $-0.1 < T_{mb} < 1.0$  K. The vertical dashed line in the spectrum indicates the position of v = 1.5 km s<sup>-1</sup> in the velocity axis.

Fig. 13.—  $^{12}$ CO(2–1) position-Velocity (p-v) diagram of the HH 315 molecular outflow, constructed by summing all spectra along an axis with a P.A.=-26° (the outflow "average" axis), over an area shown in Figure 6. The contours are 3 to 10 K in steps of 1 K, 12 to 20 K in steps of 2 K, and 25 to 85 K in steps of 5 K. The positions, along the average outflow axis, of the brightest optical emission of the six major HH knots in the flow are marked with a horizontal solid line. The thick black dash line traces the maximum contour along the

outflow axis, indicating the presumed ambient cloud gas central velocity. Notice the velocity gradient north of PV Ceph.

- 31 -

Table 1. Description of Features in the Region Surrounding HH 315

Feature	Description	Number Value or Range	See also
PV Ceph Cloud	Medium-density gas condensation associated with the formation of PV Ceph	$1.8 < v < 3.2 \text{ km s}^{-1}$ $20^{h}44^{m}32^{s} < \alpha_{1950} < 20^{h}46^{m}30^{s}$ $67^{o}36'30'' < \delta_{1950} < 67^{o}48'40''$	Figs. 4 and 5, §3.3
North Cloud	Medium-density gas condensation north of PV Ceph, associated with gas of northern outflow lobe	$0.8 < v < 2.2 \ {\rm km \ sec^{-1}}$ area same as northern outflow lobe (see below)	Figs. 5 and 6, $\S 3.3$
$v_{amb,south}$	Central velocity of ambient PV Ceph cloud gas	$2.5~\rm km~s^{-1}$	Fig. 7a, §3.3
$v_{amb,north}$	Central velocity of north cloud	$1.5~\mathrm{km~s^{-1}}$	Fig. $7b$ , $\S 3.3$
Southern lobe area	Area used to estimate the mass of the southern molecular outflow lobe	$20^{h}45^{m}10^{s} < \alpha_{1950} < 20^{h}46^{m}05^{s}$ $67^{o}41'30'' < \delta_{1950} < 67^{o}48'05''$	Fig. 6, §3.4
Northern (blue) lobe area	Area used to estimate the mass of the blueshifted molecular gas of the northern lobe	Non-square area, see Fig. 6	Fig. 6, §3.4
Northern (red) lobe area	Area used to estimate the mass of the redshifted molecular gas of the northern lobe	$20^{h}44^{m}08^{s} < \alpha_{1950} < 20^{h}44^{m}44^{s}$ $67^{o}51'30'' < \delta_{1950} < 67^{o}54'50''$	Fig. 6, §3.4

Table 2. Mass, Momentum, and Kinetic Energy of the HH 315 Molecular Outflow

	Southern Lobe		Northern Lobe			
	Redshifted gas <sup>a</sup>	If $i = 10^{\circ b}$	Blueshifted gas <sup>c</sup>	Redshifted gas <sup>d</sup>	Total	If $i = 10^{\circ b}$
Mass	1.8		4.1	0.7	$4.8~{ m M}_{\odot}$	
Momentum	$2.1 \ (\sin i)^{-1}$	12.1	$5.1 (\sin i)^{-1}$	$1 (\sin i)^{-1}$	$6.1 (\sin i)^{-1}$	$35.1~\rm M_\odot~km~s^{-1}$
Kinetic Energy	$2.9 (\sin i)^{-2}$	96	$7.6 (\sin i)^{-2}$	$1.5 (\sin i)^{-2}$	$9.1 (\sin i)^{-2}$	$302 \times 10^{43} \text{ erg}$

<sup>a</sup>We only detect redshifted gas in the southern lobe. The mass, momentum, and kinetic energy are obtained from the gas in an area shown in Figure 6, over the velocity range 3.21 < v < 6.29 km s<sup>-1</sup>.

<sup>b</sup>Value of physical parameter assuming that the angle between the plane of the sky and the outflow "axis" (i) is 10°.

<sup>c</sup>Obtained from the blueshifted gas in the area shown in Figure 6, over the velocity range -3.95 < v < 0.79 km s<sup>-1</sup>.

<sup>d</sup>Obtained from the redshifted gas in the area shown in Figure 6, over the velocity range 2.55 < v < 3.65 km s<sup>-1</sup>.

This figure "f1.jpg" is available in "jpg" format from:

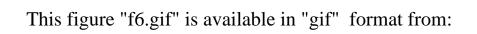
This figure "f2a.gif" is available in "gif" format from:

This figure "f2b.gif" is available in "gif" format from:

This figure "f3.gif" is available in "gif" format from:

This figure "f4.gif" is available in "gif" format from:

This figure "f5.gif" is available in "gif" format from:



This figure "f7.gif" is available in "gif" format from:

This figure "f8.gif" is available in "gif" format from:

This figure "f9.gif" is available in "gif" format from:

This figure "f10.gif" is available in "gif" format from:

This figure "f11.gif" is available in "gif" format from:

This figure "f12.gif" is available in "gif" format from:

This figure "f13.gif" is available in "gif" format from: